Breaking internal waves on sloping topography: connecting parcel displacements to overturn size, interior-boundary exchanges, and mixing

Victoria Whitley[a] and Jacob Wenegrat[a,b]

[a] *Applied Mathematics & Statistics, and Scientific Computation Program, University of Maryland, College Park*

[b] *Department of Atmospheric and Oceanic Science, University of Maryland, College Park*

Corresponding author: Victoria Whitley, whitleyv@umd.edu

ABSTRACT: Internal waves impinging on sloping topography can generate mixing through the formation of near-bottom bores and overturns in what has been called the 'internal swash' zone. Here we investigate the mixing generated during these breaking events, and the subsequent ventilation of the bottom boundary layer, across a realistic non-dimensional parameter space for the ocean using three-dimensional large eddy simulations. Waves overturn and break at two points during a wave period: when the downslope velocity is strongest and during the rapid onset of a dense, upslope bore. From the first overturning bore to the expulsion of fluid into the interior, there is a strong dependence on the length scale defined by the ratio of wave velocity over the background buoyancy frequency, an upper bound on the vertical parcel displacement an internal wave can cause. While a similar energetically-motivated vertical length scale is often seen in the context of lee wave generation over topography, the results discussed here suggest this parameter can be used to determine the size of near-boundary overturns, the strength of the ensuing turbulent mixing, and the vertical scale of the along-isopycnal intrusions of fluid ejected from the boundary layer. Consideration of a volume budget of the near-boundary region highlights spatial and temporal variability that must be taken into account when determining the water-mass transformation during this process.

1. Introduction

Internal waves breaking on topography are significant to many ocean processes. Internal tides impinging on both critical and off-critical topography can result in bottom-enhanced turbulent mixing, and diapycnal upwelling necessary for the closure of the abyssal circulation (Eriksen 1985; Polzin et al. 1997; Slinn and Riley 1998; Kunze et al. 2012; Cyr and van Haren 2016; Chalamalla et al. 2013; van Haren and Gostiaux 2012b). Recent theoretical work and observations suggest upwelling near sloping bottom boundaries may be limited to turbulent Bottom Boundary Layers (BBLs) where the mixing profile allows for convergent turbulent buoyancy fluxes, (Ferrari et al. 2016; Mashayek et al. 2017; Wynne-Cattanach et al. 2024). Exchanges between the stratified interior and the well-mixed BBL associated with breaking internal waves could be a pathway for the restratification of these boundary waters, necessary to maintain an efficient diapycnal process (Armi 1978; van Haren 2023). These breaking events and interior exchanges also allow for the transport and recycling of carbon, oxygen, and nutrients crucial for the ecosystem (Cheriton et al. 2014; Churchill et al. 1988; Bonnin et al. 2006; Cyr and van Haren 2016; McPhee-Shaw et al. 2021). The reflection and possible breaking of internal waves could result in bottom velocities strong enough to resuspend particles on the sea floor in nepheloid layers (Cacchione and Drake 1986), often observed in lakes and off continental shelves (e.g., McPhee-Shaw et al. 2004; McPhee-Shaw 2006; Bonnin et al. 2006; Edge et al. 2021). These nepheloid layers are also observed as lateral intrusions into the interior (Gardner et al. 2017; Thorpe and White 1988), similar to internal wave laboratory experiments and numerical models showing layers of dye ejected from the slope (Nokes and Ivey 1989; Winters 2015).

Several parameters have been used to characterize internal wave formation and nearby breaking in the presence of both oscillating and steady barotropic forcing, including the nonlinearity of the resulting wave behavior and the flow's ability to overcome obstacles (Winters and Armi 2013; Chalamalla et al. 2013; Sarkar and Scotti 2017; Legg and Klymak 2008; Drazin 1961). When a steady flow is blocked by topography, the length scale given by the steady velocity, U, over the buoyancy frequency, N, represents the thickness of the layer that can continue past the obstacle (Winters and Armi 2013). This results in a new "effective height," $h_{eff} = U/N$, of the topography and sets the vertical scale for the resulting waves (Winters and Armi 2013; Legg and Klymak 2008). This ratio is included in the Scorer number, as well, an atmospheric parameter characterizing lee waves (Scorer 1949). The effective height leads to the characterization of the topographic Froude number, $Fr = U/Nh$, where h is the obstacle's height. Nonlinear hydraulic effects can be found in simulations of small Fr, (Sarkar and Scotti 2017; Chalamalla et al. 2013; van Haren 2023), where the height of the obstacle is much larger than the effective height. Here we show that a similar effective height parameter is useful for characterizing aspects of wave breaking along topography.

While the generation and nearby-breaking of internal waves over topography have been extensively modeled (Winters and Armi 2013; Sarkar and Scotti 2017), there is also clear evidence of turbulence resulting from remotely forced internal waves reaching sloping boundaries (Aucan et al. 2006; van Haren et al. 2015; Jones et al. 2020). This turbulence can result from the formation of critical layers when the slope of the incident wave is close to that of the topography (Nokes and Ivey 1989; Slinn and Riley 1998; Lamb 2014; Gemmrich and Klymak 2015), but can also be found when the slope is not critical. In particular, the oscillating flow of internal waves up and down the slope can result in intermittent overturns and breaking within the phases of the wave period, sometimes described as "swashing" motions (Cyr and van Haren 2016). The overturns tend to occur at the rapid transition between down and upslope flow, as well as during the downslope phase where intensified near-slope velocities result in shear along the slope (Cyr and van Haren 2016; Aucan et al. 2006; Winters 2015; van Haren and Gostiaux 2012b; Gayen and Sarkar 2011). These types of overturning events have been observed along the continental slope (van Haren 2006) and in the deep ocean (Cyr and van Haren 2016; Wynne-Cattanach et al. 2024).

In a simulation with a low-mode internal tide impinging on a supercritical slope in rotating, stratified fluid, Winters (2015) notes a visual similarity between the length scales of the expulsion events from the boundary layer to the interior and a vertical length scale defined similarly to h_{eff} except with the velocity scale set by the wave velocities (rather than a steady background flow)—a quantity we term here as the *effective wave height*. A similar dependence on the effective wave height was also noted to scale the size of turbulent patches in Large Eddy Simulations (LES) of internal tides interacting with the steep western ridge of the Luzon strait (Jalali et al. 2017). Motivated by these observations and results this paper focuses on a set of highly-resolved, three-dimensional simulations of internal waves impinging on sloping boundaries, where wave velocity, stratification, frequency, and criticality are varied, spanning a range of values relevant to the ocean. There is a strong dependence on the vertical effective wave height throughout the breaking process,

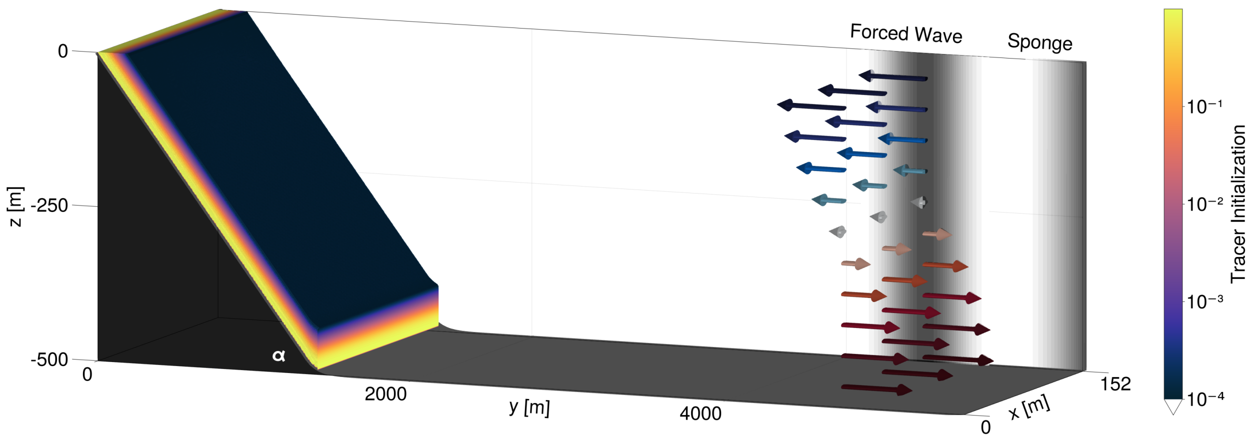

FIG. 1. 3D LES domain set up. Planar topography with slope $\tan\alpha$ shown in black. The location of the forced internal wave is indicated with arrows centered at $y = 4500$, and the gray Gaussian shading behind the arrows. The sponge regions near the right boundary are also marked out with gray shading, representing the amplitude of damping. Contours of the initial hyperbolic tangent condition of the concentration of the tracer are also shown. The tracer is uniformly initialized in the across-slope direction, similar to the topography.

resulting in subsequent dissipation and boundary-interior exchange scaled by the effective wave height near the slope.

The manuscript is organized as follows. In section 2 we introduce the high-resolution model used to explore the breaking events as well as a description of the parameter space surveyed in this study. In section 3 we describe a characteristic breaking event and introduce the governing scaling found throughout the mixing process. This is followed by an explanation of the mechanism behind the resulting interior and boundary exchange with connections to the previously discussed vertical scaling. Water-mass transformation and diapycnal mixing involved are then analyzed for a representative simulation. Conclusions, and several avenues for future study, are reviewed in section 4.

2. Numerical Model Set Up

To explore the interaction between the BBL and the interior in the presence of breaking internal waves, we used high-resolution Large Eddy Simulations (LES) of internal waves impinging on a planar slope. The incompressible Navier-Stokes equations under the Boussinesq approximation were solved using a non-hydrostatic model in the julia package, Oceananigans (Ramadhan et al.

2020). Oceananigans uses a finite volume method on a staggered, structured grid based on that of MITgcm (Ramadhan et al. 2020; Marshall et al. 1997). A fifth-order weighted essentially non-oscillatory (WENO) scheme advects velocities and tracers, with a third-order Runge–Kutta time-stepping method (Ramadhan et al. 2020; Silvestri et al. 2024). A Fast Fourier Transform solves Poisson's equation for the non-hydrostatic pressure (Ramadhan et al. 2020). We employed the Smagorinsky-Lilly subgrid-scale model for the LES turbulence closure, with a turbulent Prandtl number, $Pr_t = 1$. With an average eddy viscosity of O(10^{-3} m^{2}s^{-1}) and Reynolds number of O(10^5), background molecular diffusivity and viscosity were omitted from the model.

The domain, shown in Fig. 1, is three-dimensional, with size $(L_x, L_y, L_z) = (152, 6500, 500)$ m, with periodicity in the along-isobath (x) direction and uniform grid spacing of $\Delta y = \Delta x = 4$ m and $\Delta z = 2$ m. To test the grid resolution dependency, vertical grid spacing was varied from $\Delta z = 1.5$ m to 6 m, and the horizontal spacing from $\Delta x = \Delta y = 3$ m to 8 m, for two representative simulations. The chosen grid spacing, $\Delta y = \Delta x = 4$ m and $\Delta z = 2$ m, was found to resolve the Ozmidov length, defined as,

$$L_O = \Big(\frac{\bar{\epsilon}}{N_0^3}\Big)^{1/2}, \tag{1}$$

where $\bar{\epsilon}$ is the average dissipation rate of kinetic energy over turbulent regions, ($\epsilon > 10^{-10}$ m^{2}s^{-3}) (Khani 2018; Dillon 1982). Other results discussed in this paper, such as average intrusion thicknesses and the buoyancy flux analysis were also found to be quantitatively insensitive to the changes in resolution, as long as the prevailing length scales were resolved with several grid points. The behavior of the simulations with the largest expected characteristic length scales could be impacted by the limitations of the vertical domain. To check this, three simulations were run with an increased vertical height of $L_z = 650$ m. These simulations are marked by $(\cdot)^+$ in Table 1 and denoted by $(\cdot)^B$ in the corresponding results.

Boundary conditions in the bottom normal direction were no flux on buoyancy and tracers and quadratic drag on momentum. Topography was included in the simulation using a grid-fitted immersed boundary method with the quadratic drag boundary conditions set on each boundary-adjacent cell face. The idealized domain was initialized with a uniform stratification, N_0^2, and constant Coriolis frequency, f, with the ratio, $N_0/f = 10.7$, kept constant over all simulations. The topographic slope was given by $\tan\alpha$. A full list of parameters for the main set of simulations can be found in Tables 1 and 2.

Table 1. Simulation Parameters for Main Reference Set

	Vary V_0			Vary N_0		
h_w	V_0	N_0^2	L_z	V_0	N_0^2	L_z
[m]	[ms^{-1}]	[s^{-2}]	[m]	[ms^{-1}]	[s^{-2}]	[m]
14.29	0.05	1.23×10^{-5}	500	0.25	3.06×10^{-4}	500
28.57	0.10	1.23×10^{-5}	500	0.25	7.66×10^{-5}	500
42.86	0.15	1.23×10^{-5}	500	0.25	3.40×10^{-5}	500
57.14*	0.20	1.23×10^{-5}	500	0.25	1.91×10^{-5}	500
71.43	0.25	1.23×10^{-5}	500	0.25	1.23×10^{-5}	500
85.71	0.30	1.23×10^{-5}	500	0.25	8.51×10^{-6}	500
100.00**	0.35	1.23×10^{-5}	500	0.25	6.25×10^{-6}	500
114.29	0.40	1.23×10^{-5}	500	0.25	4.79×10^{-6}	500
128.57	0.45	1.23×10^{-5}	500^{+}	0.25	3.78×10^{-6}	500
142.86	0.50	1.23×10^{-5}	500^{+}	0.25	3.06×10^{-6}	500
157.14	0.55	1.23×10^{-5}	500^{+}	0.25	2.53×10^{-6}	500

*Similar to the values used in Winters (2015)

**Similar to the values observed in van Haren (2006)

$^{+}$Simulations also run with L_z = 650 m for Vary V_0^B case

Table 2. Constant Simulation Parameters for Main Reference Set

Parameter	Value	Comment
N_0/f	10.7	Chosen for comparison to Winters (2015)
σ/f	2.2	$\sigma/f > 2$, PSI possible
h [m]	500	Height of topography
$\ell[m]$	1406	Length of topography
$\tan\alpha$	0.356	Topographic slope ($\mathrm{d}h/\mathrm{d}\ell$)
γ	1.9	Slope is supercritical ($\tan\alpha/\tan\theta$)

The exchange of fluid between the lower boundary layer and the interior was quantified using a passive, neutrally buoyant, tracer initialized along the entire slope boundary using a hyperbolic tangent function extending 20 m above the slope. This initialization can also be seen in Fig. 1. The change in integrated tracer volume in the model compared to the initial volume was on the order of 10^{-10} for all simulations, indicating the immersed boundary method used in Oceananigans conserved the dye for this simulation setup sufficiently for the purposes of the following analyses.

In each simulation, mode-1 oscillations were continuously forced in the v momentum equation. The forcing region was determined by a Gaussian centered at $y = 4500$ m, more than 3000 m from the closest point of the slope, as seen in the arrows and gray contours in Fig. 1. The forcing was

TABLE 3. Simulation Parameters for Assessing Sensitivity to Wave Frequency, σ, and Criticality, γ

Vary γ						
h_w [m]	V_0 [ms^{-1}]	N_0^2 [s^{-2}]	N/f	σ/f	γ (tan α/tan θ)	tan α (dh/dx)
42.86	0.15	1.23×10^{-5}	10.7	2.8	1.4	0.356
42.86	0.15	1.23×10^{-5}	10.7	5.5	0.6	0.356
128.57	0.45	1.23×10^{-5}	10.7	2.8	1.4	0.356
128.57	0.45	1.23×10^{-5}	10.7	5.5	0.6	0.356

derived by taking the v component from linear internal wave theory as

$$v(x,y,z,t) = V_0 \cos(ly + mz - \sigma t), \tag{2}$$

with maximum velocity, V_0, and frequency, σ, specified in each simulation. The horizontal wave number, l, was determined from the dispersion relation for linear internal waves (Gill 1982). Simulations were run with mode-1 vertical wave number, $m = \pi/L_z$, representative of an internal tide. Using only the v component was found to be sufficient to set up an oscillating internal wave, with resulting velocities close to the prescribed V_0. Typically, tidal velocities would be a few centimeters per second, although this was varied here from 0.05 ms^{-1} to 0.55 ms^{-1} to span a wide range of the parameter space (Table 1). The wave period, $T_\sigma = 2\pi/\sigma$, from the forced wave, will be used to describe some simulation results. All simulations were run for at least 11 wave periods, with a variable time step between 10^{-4} s and 10 s, as determined by a CFL of 0.5 within the simulation. Diagnostics were calculated every 600 s, or such that there are at least 15 snapshots every wave period. A sponge region was added to all fields along the right boundary of the domain to prevent spurious reflections (sponge region marked with gray contours in Fig. 1).

While varying the buoyancy frequency and wave velocity, some relationships were held constant (Table 2), using values from Winters (2015). The slope of internal wave propagation is given by,

$$\tan\theta = \sqrt{\frac{\sigma^2 - f^2}{N^2 - \sigma^2}}. \tag{3}$$

For the main set of simulations, a criticality of $\gamma = \tan\alpha/\tan\theta = 1.9$ was used. While the slope used in these simulations was physically steep due to computational limitations, the criticality is within

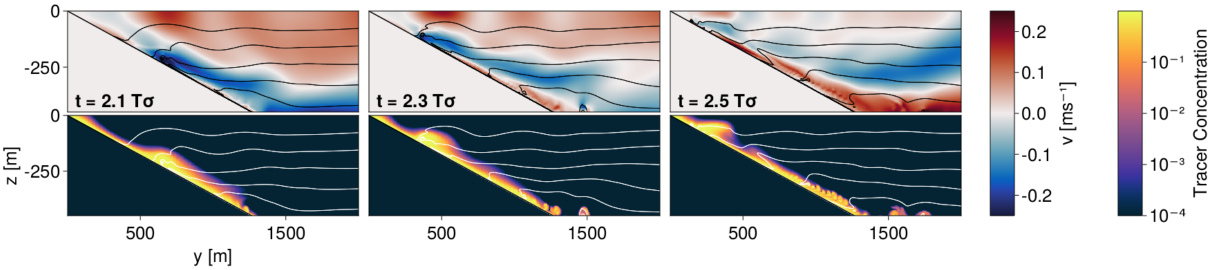

FIG. 2. Snapshots of velocity (v, top row) and dye concentration (bottom row) during the second wave period. The right column, $t = 2.5\,T_\sigma$, shows the initial small overturns found along the slope during this quasi-spin-up period. Isopycnals are marked as contour lines in all images. Animations can be found of these fields in the supporting information.

the range of observed values (see for instance van Haren 2006; Wynne-Cattanach et al. 2024), and results were tested and found to be qualitatively insensitive to the chosen ratio of $\tan\alpha/\tan\theta$ for another supercritical and also a subcritical value. The ratio $\sigma/f = 2.2$ was held constant for the simulations in the main parameter space of Table 1, while the additional cases of subcritical and supercritical wave reflection were tested by varying the ratio σ/f, but holding N/f constant, as shown in Table 3. All parameter values varying σ and γ still followed the relationships found for the supercritical results with $\sigma/f = 2.2$.

3. Results

a. Physical mechanism and scaling of breaking internal waves

Snapshots from the first breaking event above a supercritical slope ($\tan\alpha/\tan\theta = 1.9$), with velocity, $V_0 = 0.25$ ms^{-1}, and stratification, $N_0^2 = 1.23\times10^{-5}$ s^{-1} are shown in Fig. 2. The simulation was started from rest, except for the incoming forced wave. Initially, the internal wave advected isopycnals along the slope. During the second wave period ($t = 2\ T_\sigma$) a bore of denser water was formed and advected up the slope, shown in Fig. 2 ($t = 2.1T_\sigma$). Halfway through this upslope phase, the water closest to the slope in the lower 20 meters began to advect back down the slope (Fig. 2, $t = 2.3T_\sigma$). Convective instability near the boundary during the wave phase transition resulted in small overturns, with downslope flow carrying lighter water near the boundary while the upslope phase still carried denser water aloft, as seen in Fig. 2 ($t = 2.5T_\sigma$). These initial overturns

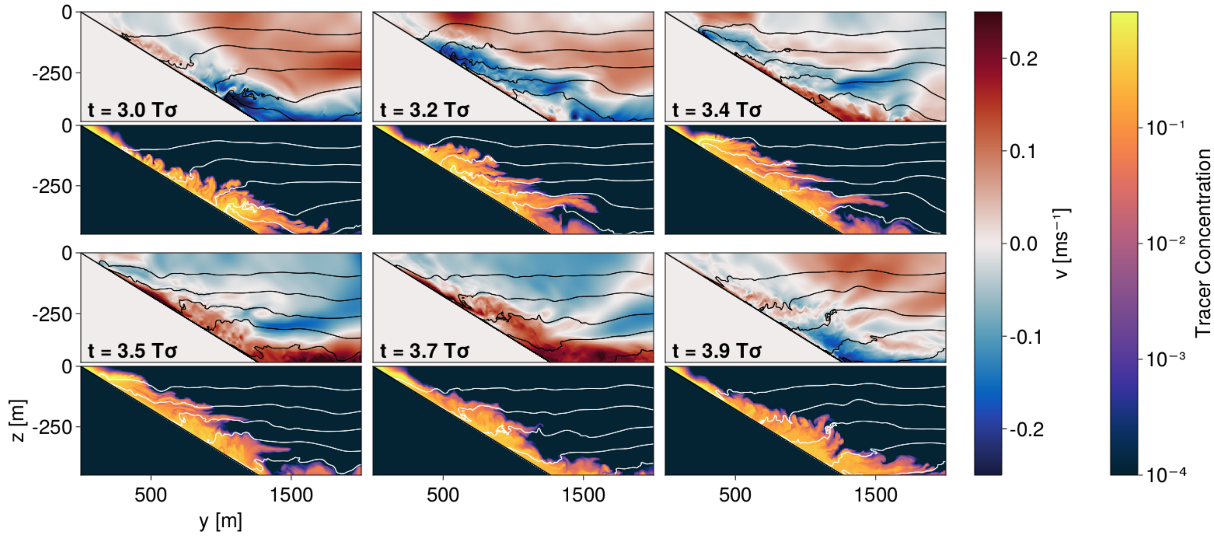

FIG. 3. Snapshots of velocity (v, first rows) and dye concentration (secondary rows) during the third wave period. The upper left plots, $t = 3.0T_\sigma$, show the initial large upslope bore (blue). Isopycnals are marked as contour lines in all images. Animations can be found of these fields in the supporting information.

were similar to those described in low amplitude velocity cases (Drake et al. 2020; Kaiser et al. 2022), but this phasing was here only characteristic of those initial few wave periods and is not the focus of this work.

Following these initial small breaking events in the same simulation, the characteristic overturning process depicted in Fig. 3 is representative of the evolution seen across the surveyed parameter space. At the beginning of the upslope phase, a much larger bore of dense water immediately overturned and broke along the slope around 300 m depth (Fig. 3, $t = 3.0 - 3.2T_\sigma$). This was followed by smaller overturns at the transition to downslope flow ($t = 3.4T_\sigma$), similar to those discussed in the earliest wave periods. However, these were not as significant as the second overturn event which occurred when downslope flow was at a maximum, bringing lighter water under heavier water, as seen at $t = 3.5 - 3.7T_\sigma$ in Fig. 3. Similar downslope overturns observed in the Kaena Ridge, and in LES have been attributed to shear instability (Aucan et al. 2006; Gayen and Sarkar 2011). The bore leading a sharp transition to upslope flow, and the intensified flow near the boundary during the downslope phase, often accompanied by an increase in turbulence and mixing, have been found in both numerical simulations and observations of tidal flow over steep topography (Cyr and van Haren 2016; Aucan et al. 2006; Winters 2015; Gemmrich and Klymak 2015; Slinn and

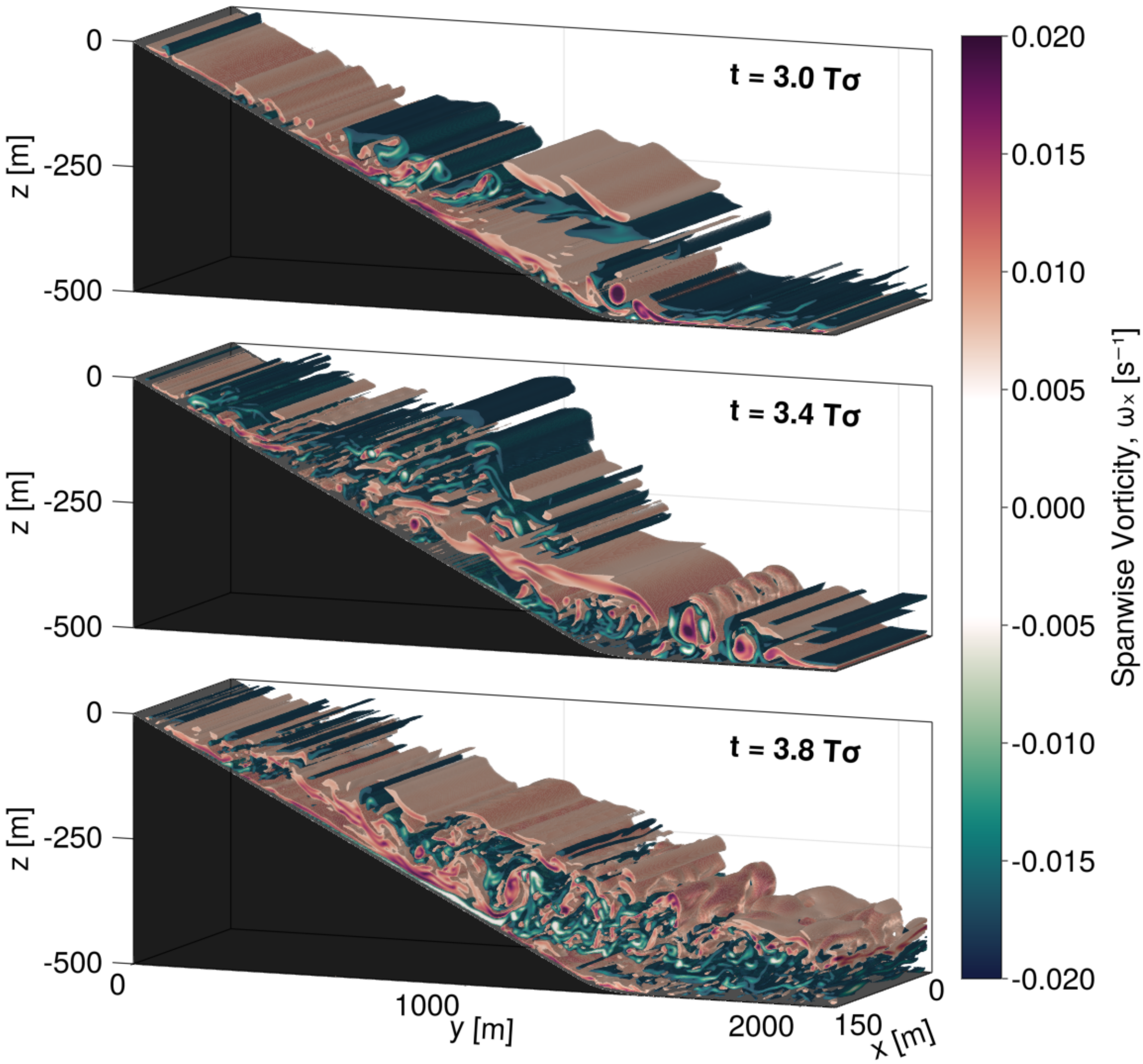

FIG. 4. 3D contours of the spanwise (ω_x) component of the vorticity for the same simulation in Fig. 3. Values shown at three points within the wave period indicate the development of 3D structures and the transition to turbulence. An animated version of this figure is available in the supplementary material.

Riley 1998). As the transition to upslope flow was particularly rapid, the upslope bore often directly interacted with the downslope overturns in these simulations. The velocity structure in the interior, away from the mixing zone, also showed signs of wave reflection off the slope and the domain walls in Fig. 3. These competing velocities created multi-layered gravitational instabilities resulting in even larger overturns and more mixing. The spanwise vorticity for the same simulation shows the transition to three-dimensional turbulence during this wave period (Fig. 4). Along-slope vortices developed, with across-slope variations at the transition between up and downslope flow (Fig. 4, $t = 3.4T_\sigma$). The downslope breaking event caused an increase in turbulence, with smaller-scale structures appearing, and more regions of high vorticity developing along the slope. This process continued with two overturning and mixing events during each wave period, though following wave periods start with pre-existing three-dimensional structures instead of the two-dimensional overturning features seen at $t = 3.0T_\sigma$ in Fig. 4.

A survey of simulations with velocities ranging from $V_0 = 0.05$ to 0.55 ms^{-1} and stratifications between $N_0^2 = 2.56 \times 10^{-6}$ and 3.6×10^{-4} s^{-1}, showed the bores, overturns, and, consequently, breaking events along the slope all follow similar patterns as described above. However, a small set of simulations run with subcritical slopes, small magnitudes of velocity, $V_0 = 0.05$ ms^{-1}, or strong initial stratification, $N_0^2 = 3.6 \times 10^{-4}$ s^{-1}, did not always show these same general characteristics and breaking events, as topographic interactions remained linear and stably stratified (Klymak et al. 2012; Balmforth and Young 2002). Smaller velocities or stronger stratification could not be tested, since the grid resolution would not be able to capture the necessary turbulent scales in these cases.

We focus analysis in particular on the importance of what we term the *effective wave height*,

$$h_w = \frac{V_0}{N_0}, \tag{4}$$

where again V_0 is the magnitude of the wave velocity and N_0 is the interior buoyancy frequency (note that this parameter was denoted δ in Winters 2015). This height scale is analogous to h_{eff} but scales with the wave velocity itself rather than with the steady interior flow. It can thus be interpreted physically as the largest vertical distance a water parcel can be moved before losing all of its wave kinetic energy to potential energy (Winters 2015; Winters and Armi 2013). Below we show the effective wave height parameter organizes many of the simulation results across a wide range of V_0 and N_0 values, spanning h_w values from 14.3 to 157.1 m (Table 1). Both V_0 and N_0 values were varied to produce the same range of h_w (Table 1), ensuring the scaling relationships identified were due to the effective wave height and not changes in the wave velocity or stratification alone.

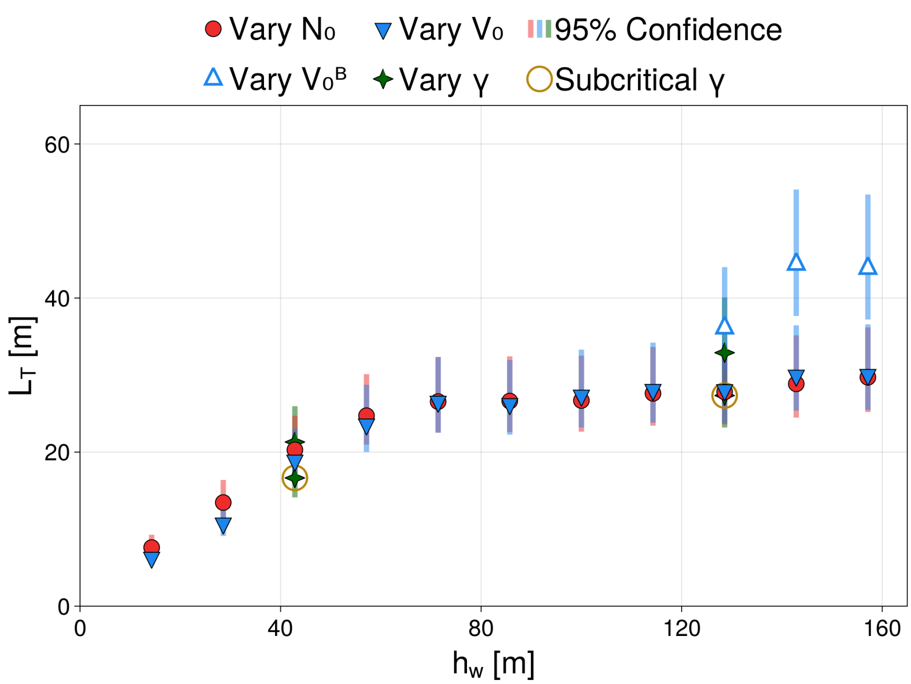

FIG. 5. RMS Thorpe Scale, L_T, for each simulation is related to h_w. Simulations varying the slope criticality, γ, hold N constant for two V_0 values, shown by the green stars, including for subcritical cases (gold rings). Simulations with the largest overturns have some domain dependence, as seen in the simulations with added vertical domain, V_0^B. Error bars indicate 95% confidence intervals on exponential distributions.

Since the effective wave height is a constraint on a parcel's vertical displacement, h_w is expected to set an upper bound on the wave overturn size. Overturns can be measured with the Thorpe scale (Thorpe 1977), defined as the root mean square (RMS) of the displacement necessary to adiabatically reorder the buoyancy profile to make it gravitationally stable. Overturns estimated from the simulations were only counted if the buoyancy range within the overturn exceeded a threshold of $\Delta b > 2\Delta z N_0^2$ and the length scale $L_T > 2\Delta z$ to avoid spurious identification of overturns not resolved by the numerical grid. Thorpe scale has often been used as a way of estimating the available potential energy from a mooring profile (van Haren and Gostiaux 2012a; McPhee-Shaw and Kunze 2002; Jones et al. 2020), though its efficacy is dependent on assumptions of the type of turbulence and overturns being measured (Jalali and Sarkar 2017; Dillon 1982; Mater et al. 2013). Instead, in these results the effective wave height, h_w was compared directly to the average Thorpe scale, L_T, as a bulk direct measure of overturn size within each of the simulations.

This relationship between the effective wave height and the resulting Thorpe average for each simulation is shown in Fig. 5. There was an approximately piecewise-linear relationship between h_w and L_T, with little difference between the simulations where V_0 was varied as compared to N_0 varied, suggesting that the simple measure of the effective wave height effectively scaled the breaking events near the boundary. The small differences in overturn size for large h_w simulations could be a domain dependence on the calculation of Thorpe scale as h_w approaches 100 m. A set of simulations, V_0^B, where the vertical domain was increased by 150 m resulted in an increase in the measured L_T, consistent with this interpretation. The plateau in these averaged results also heavily sampled an increasing number of small overturns present alongside the larger overturn events discussed earlier. Therefore, the effective wave height could still be controlling the size of the largest parcel displacements, and thereby the most energetic overturns, while the RMS estimate of Thorpe scale remained smaller. Such a domain dependence could have implications for the relevance of this scaling in shallow coastal waters, but here we focus on applications similar to the abyssal setting, where h_w and overturning features are much smaller than the depth.

b. Overturns and dissipation in breaking waves scaled by h_w

The approximate relationship between L_T and h_w suggests that the effective wave height usefully scales the bulk overturning size. This suggests that the dissipation rate may be inferred from h_w, in the same manner that dissipation rate is often inferred from L_T (Dillon 1982; Mater et al. 2015). This approach is based on an assumption of near-constant Richardson number which gives that $L_O = CL_T$, where C is an order-1 constant, and L_O is the Ozmidov scale (Dillon 1982). The Ozmidov scale, L_O (Hopfinger 1987), gives the size of the largest eddy not dampened by buoyancy (McPhee-Shaw and Kunze 2002; Jalali et al. 2017), and is directly related to the dissipation rate by,

$$L_O^2 = \epsilon/N^3. \tag{5}$$

Thus, the turbulent dissipation rate can be estimated as $\widehat{\epsilon} \approx C^2 L_T^2 N^3$, where the carat notation is used to indicate an approximated quantity. The often-used constant value $C = 0.8$ (Dillon 1982) results in the relationship $\widehat{\epsilon} \approx 0.64 L_T^2 N^3$. This connection between Thorpe scale and dissipation rate has been taken advantage of in observations where overturns can be quantified in profile data,

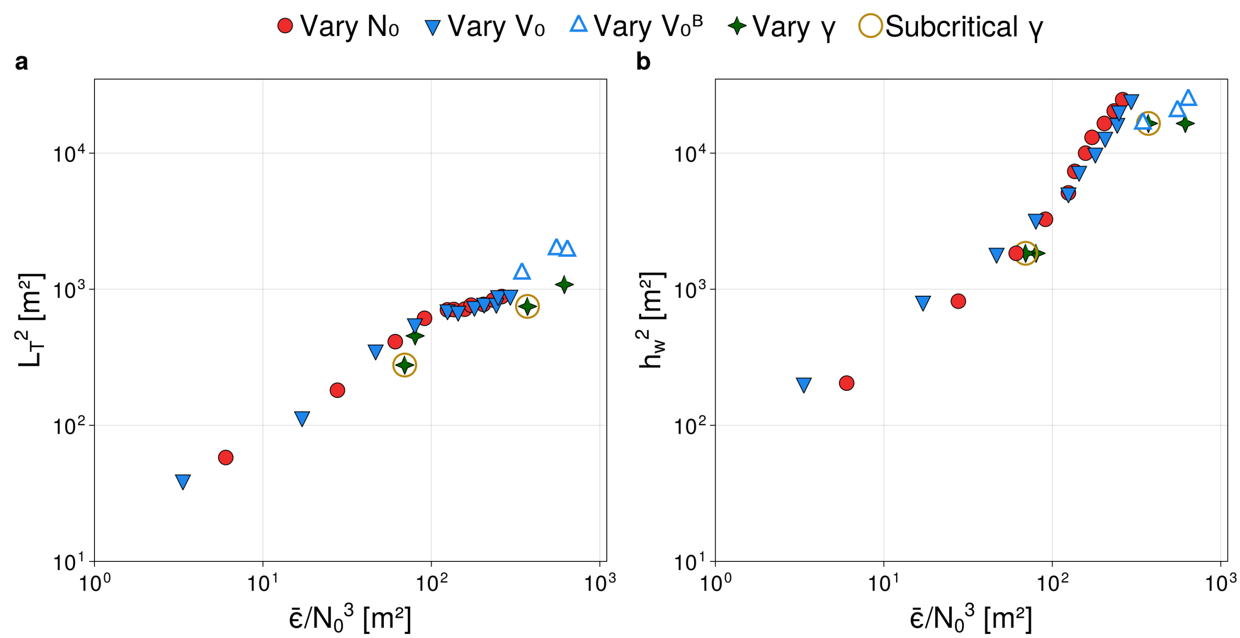

FIG. 6. Ozmidov scale, using the average dissipation over waves 6-10, is compared to Thorpe Scale (a) and h_w (b). Results are shown for simulations that vary V_0 (solid blue markers), holding $N_0 = 3.5 \times 10^{-}3$, and vary N (solid red markers), holding $V_0 = 0.25$ ms^{-1}. Simulations varying slope criticality (solid green markers) and increased domain size (open blue markers) also show a similar relationship.

including those of convective and shear-driven overturns near topography, (Alford et al. 2011; van Haren and Gostiaux 2012a; Legg and Klymak 2008; Cyr and van Haren 2016).

The relationship between the squared Ozmidov scale and the squared Thorpe scale is shown in Fig. 6a for varying simulations, where $\bar{\epsilon}$ is the average dissipation, calculated from model fields as

$$\bar{\epsilon} = \overline{\nu_e \left(\frac{\partial u_i}{\partial x_j}\right)\left(\frac{\partial u_i}{\partial x_j}\right)}. \tag{6}$$

ν_e is the eddy viscosity and $\overline{(\cdot)}$ denotes averaging over wave periods 6 through 11. The Ozmidov scale in Fig. 6, was calculated using (5), where N was determined by the initial buoyancy frequency, N_0. As expected, the Thorpe-scale estimates of the dissipation rate reasonably approximated the true dissipation rate across more than two orders of magnitude. The Thorpe and Ozmidov relationship had a shallower slope at high dissipation rates, due to the same change in slope seen in Fig. 5. This flattening was less pronounced for simulations with additional vertical domain size (*Vary* V_0^B), suggesting (as above), some potential dependence on the computational domain for the largest wave velocities ($V_0 > 0.4$ ms^{-1}) and weakest stratification ($N_0 < 2.1 \times 10^{-3}$ s^{-1}).

A similar relationship can be found by replacing the Thorpe scale with the effective wave height, as a simple approximate measure of the bulk overturn size. This gives, $L_O^2 \approx C' h_w^2$, such that the dissipation rate can be approximated using only the wave velocity magnitude and buoyancy frequency,

$$\widehat{\epsilon} \approx C' h_w^2 N_0^3. \tag{7}$$

The relationship between Ozmidov scale calculated using the average dissipation rate and the effective wave height for the simulations is shown in Fig. 6b, with a best-fit coefficient of $C' \approx 0.02$ over all simulations. Bursts of dissipation of kinetic energy rate on the order of 10^{-6} m^{2}s^{-3} observed near breaking internal waves in the Rockall Trough match with the estimate using (7), given their approximately measured stratification of 3×10^{-6} s^{-1} and wave velocity of 0.2 ms^{-1}, which together imply and an h_w of 115 m (Wynne-Cattanach et al. 2024; Alford et al. 2024). However we emphasize that this agreement may be simply fortuitous, and we do not claim this empirical relationship will always generalize, especially given the inherent variability found here and in observational estimates, as well as complexities of realistic bathymetry (discussed further in section 4). However, in the simulations considered here, h_w captured the impact of both changes in the wave velocity magnitude and initial buoyancy frequency on breaking events, including for the simulations with different slope criticality. Since $h_w^2 = V_0^2/N_0^2$, there is a dependence on N_0 in both the Ozmidov scale and effective wave height, albeit appearing at different polynomial orders. Increasing the vertical domain size reduced the steepness in the velocity-varying results, indicating the same dependence on the domain as Fig. 6a. These results, along with those of section 3a, indicate that the simple scaling parameter h_w effectively captures the bulk overturning size during these wave breaking, and hence also can be used to characterize the ensuing turbulent dissipation of kinetic energy.

c. Boundary layer and interior exchange through adiabatic pumping

The presence of turbulence and overturns near sloping boundaries alone does not mean breaking internal waves necessarily generate efficient mixing. To maintain efficient mixing along sloping

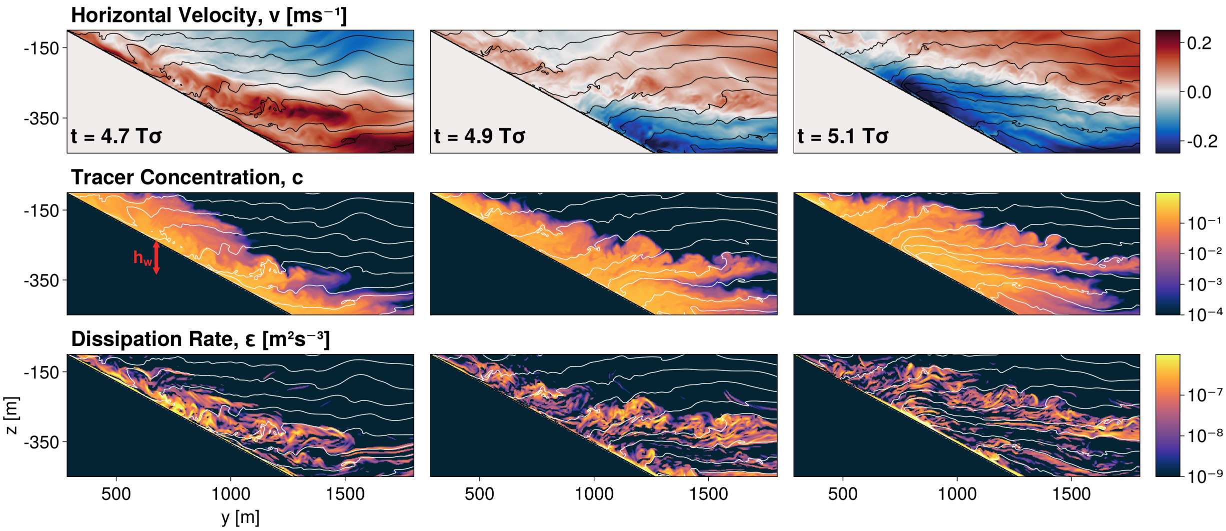

FIG. 7. Horizontal velocity, slope-initialized tracer, and dissipation of kinetic energy rate during an ejection event. Isopycnals in intervals of $\Delta b = 5 \times 10^{-4}$ marked in all images. At the end of the downslope breaking event at wave period 4.7, the water is mixed within one h_w of the slope (marked in red). The upslope bore shown at wave periods 4.9 and 5.1 eject tracer into the interior (section 3c).

boundaries, there needs to be a pathway for the restratification of the BBL. Understanding the exchange process requires a closer look at the temporal and spatial variations within these simulations, rather than only the integrated metrics discussed in the previous results. The breaking of internal waves on the downslope phase created well-mixed boundary waters right before the upslope phase began, over a vertical scale limited by the effective wave height, h_w. The incoming dense bore was led by a region of strong buoyancy gradients, visible in the collapsed isopycnals in Fig. 7. The presence of the strong downslope velocity from the previous overturn phase, coupled with the incoming dense bore, caused an ejection of the newly mixed boundary waters along the isopycnals into the interior. These intrusions can be seen in Fig. 7, through the slope-initialized dye and regions of increased dissipation of kinetic energy rate being expelled at $t = 5.1\ T_\sigma$. Fig. 8 shows three-dimensional snapshots after the tracer has been ejected into the interior (for a simulation with $h_w = 100$ m, the reader is referred to animations in the supporting information to help build further physical intuition). Over the course of a wave period, the tracer was pumped back and forth from the boundary, as indicated by the tendrils extending into and retracting from the

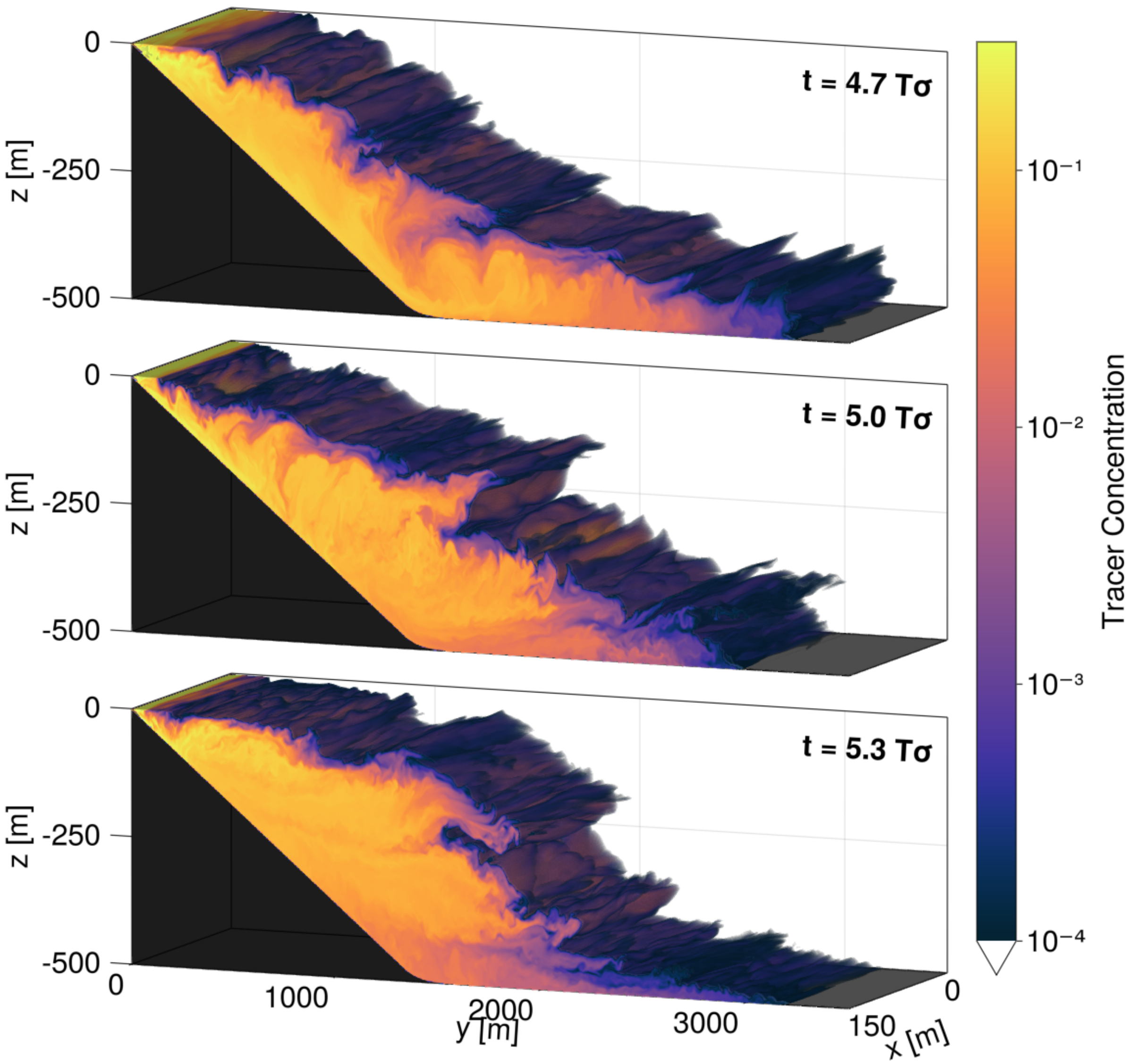

FIG. 8. 3D contours of slope initialized passive tracer concentration (log scale) for simulation with $V_0 = 0.35$ ms^{-1}, $N_0 = 3.5 \times 10^{-3}$ s^{-1}, and $h_w = 100.00$ m. Concentrations less than 10^{-4} are omitted. Values are shown at three points across the 4th and 5th wave period. Tracer is laterally ejected, extending 2500 m into the interior at $t = 5.0T_\sigma$, the transition between up and downslope flow. A 3D animation can be found of this ejection process in the supporting information.

interior. Such ejections and layers of increased turbulence or materials are often seen in numerical simulations, lab experiments, and observations (Cyr and van Haren 2016; McPhee-Shaw 2006;

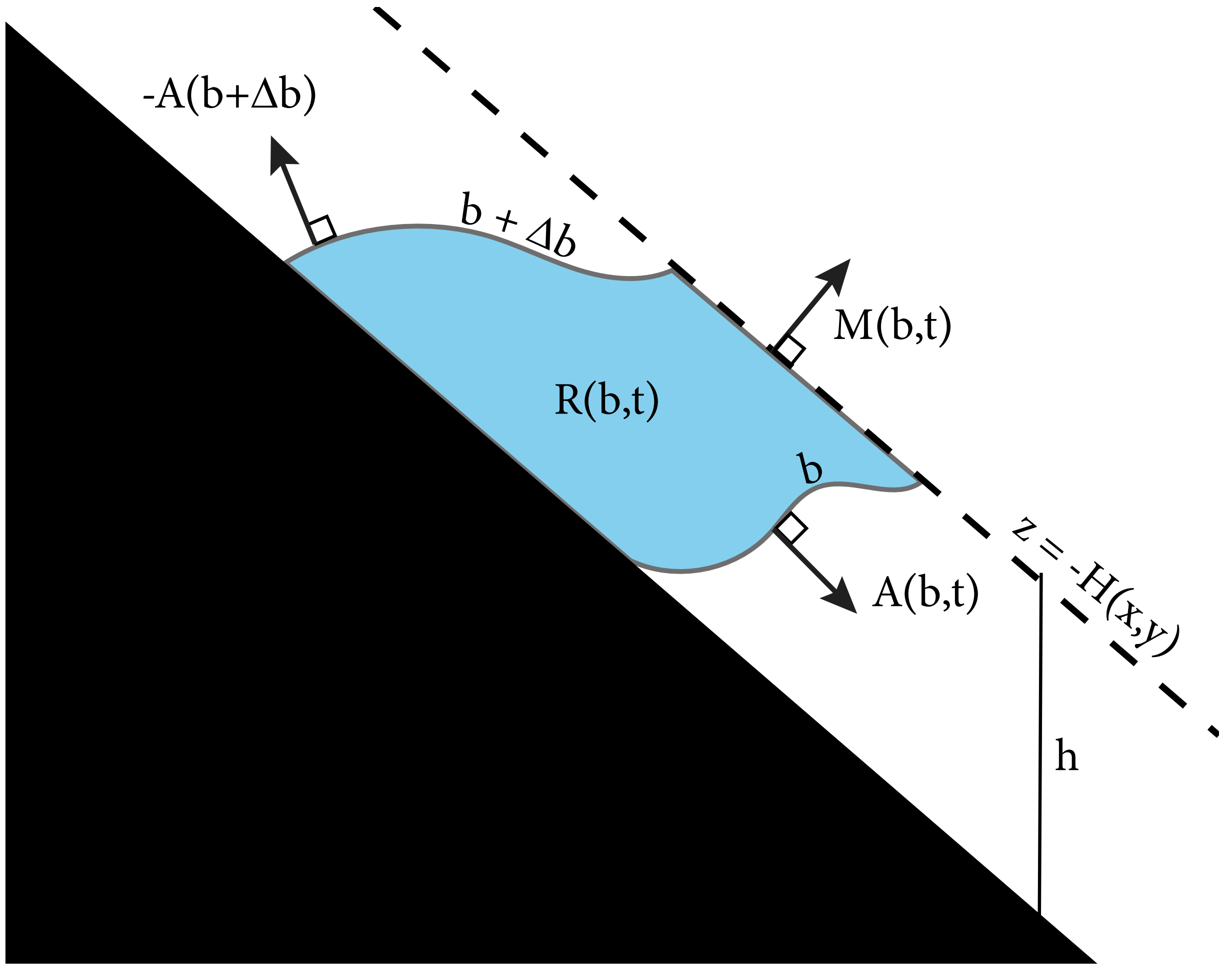

Fig. 9. Shaded volume bounded by two isopycnals, the topography, and the fixed surface $H(x, y)$. $H(x, y)$ is a vertical distance of $h = 1.1h_w$ from the slope. The diapycnal volume flux through the isopycnal surfaces is A and the flux through H into the interior is M (Marshall et al. 1999).

Edge et al. 2021; Nokes and Ivey 1989; Winters 2015; van Haren 2023; Wynne-Cattanach et al. 2024; McPhee-Shaw et al. 2021).

The timing of the exchange process can also be seen by looking at phase-averaged Hovmöller plots of the near boundary region in buoyancy space. Each buoyancy class represents a region, $R(b,t)$ of size $\Delta b = 20\ N_0^2$ within $1.1\, h_w$ of the sloping topography, creating 25 initially equal volumes. The diagram in Fig. 9 indicates such a region shaded in blue. Fig. 10 takes the phase average over waves 4 through 10 of a representative simulation. The first row shows the average horizontal velocity (a), dissipation of kinetic energy rate (b), and stratification anomaly (c) in each

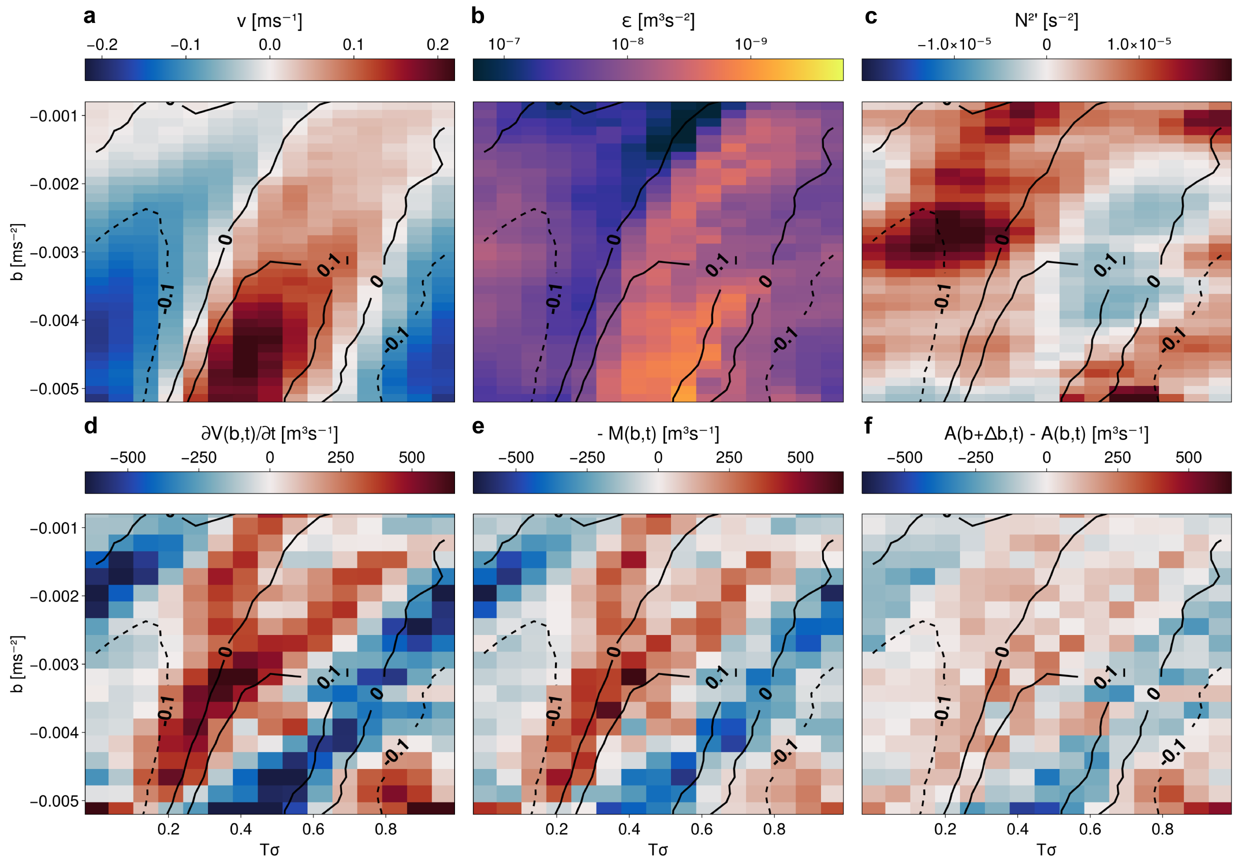

FIG. 10. Representative simulation with $V_0 = 0.35$ ms^{-1}, $N_0 = 3.5\times10^{-3}$ s^{-1}, and $h_w = 100.00$ m. Row one shows the average (a) horizontal velocity, (b) dissipation of kinetic energy rate, and (c) stratification anomaly in each buoyancy bin. Row two is the buoyancy binned volume budget within $1.1h_w$ of the slope (refer to Fig 9 and Eq. 8): (d) the buoyancy class volume rate of change, (e) the flux of volume from the interior, (f) the flux through the isopycnal surfaces, calculated as the residual of (e) and (f). All are phase averaged over waves 4 - 10. Contours show the average horizontal velocity in each buoyancy class, indicating the ejections into the interior occur at the transition between up ($v < 0$) and downslope flow ($v > 0$). Dissipation rate is strongest, while stratification is weakest, during the downslope phase.

buoyancy class during a wave period. The upslope phase replenished the boundary with strong stratification, while the downslope phase had increased dissipation and weak stratification, directly before the ejection. This phasing difference, with dissipation rate and stratification inversely varying, has also been seen in simulations of barotropic tides (Ruan and Ferrari 2023; Gayen and

Sarkar 2011) as well as in observations (Cyr and van Haren 2016; Nielson and Henderson 2022; Aucan et al. 2006).

The near boundary volume of a specific buoyancy class will only be altered by the diapycnal fluxes through the isopycnal surfaces bounding the class, $A(b+\Delta b) - A(b)$, and volume fluxes into the interior, $M(b)$ (Marshall et al. 1999). The volume budget of a buoyancy class, $R(b,t)$, bounded by b and $b+\Delta b$, is given by,

$$\frac{\partial V(b,t)}{\partial t} = A(b+\Delta b,t) - A(b,t) - M(b,t) \tag{8}$$

These terms are compared in Fig. 10, where positive values indicate an increase in boundary volume. The contraction and dilation of the near boundary buoyancy classes occurred at the transitions between wave phase, (along the $v = 0$ ms^{-1} contours). These changes in near-boundary volume were largely balanced by the volume fluxes into and out of the interior. At the transition between downslope ($v > 0$) and upslope ($v > 0$) flow the loss of volume near the boundary was accompanied by a flux of volume into the interior ($-M(b,t) < 0$), indicating an adiabatic pumping process, creating the exchange between the boundary and interior. While most of the change in volume close to the slope was due to adiabatic motions, the residual between the $\partial V/\partial t$ and $-M$ was not negligible, indicating there were also irreversible changes due to diapycnal volume flux through isopycnal surfaces, $A(b+\Delta b) - A(b)$ during the exchange process, to be discussed more in section 3d.

The exchange of fluid between the boundary layer and interior was quantified using the passive tracer initialized along the slope (eg. Fig. 1). The along isopycnal ejections took the form of tendrils of high concentration extending into the interior (Figs. 7, 8). For each simulation, we calculated an average (and median) tracer intrusion vertical thickness L_{tr}. Details of the method and associated uncertainty are given in Appendix A, with an example calculation in the associated Fig. A1. The thickness of these layers in the interior scaled approximately 1-1 with h_w, as shown in Fig. 11a. We emphasize that there was significant variability in tracer intrusion sizes with each simulation, both as a function of space (distance along the slope) and wave phase. Using the tracer thickness diagnostic method on observations indicated a similar amount of variability. Intrusion thicknesses of dissolved oxygen anomaly as a passive tracer in the Monterrey canyon ranged from $50-160$ m with a similar span in estimated effective wave height from observed stratification

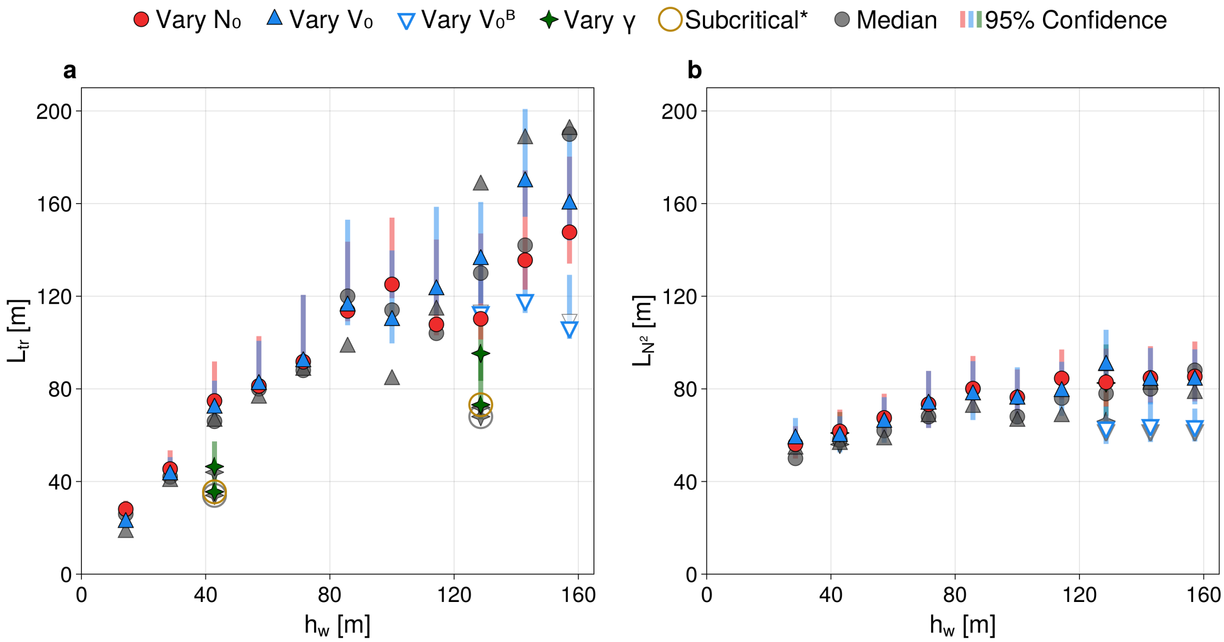

FIG. 11. Comparing h_w to the thickness of the dye intrusions away from the slope (a) and the thickness of the layers of weak stratification anomalies (b). 95th confidence intervals are included for all simulations as error bars. Medians for each simulation are included in gray. A linear relationship of order 1 holds over simulations that vary V_0 and N_0, as well as varying the slope criticality. Subcritical simulations are not shown in panel b, as linear wave dynamics made it difficult to identify well-mixed regions using this method (Appendix B). Error bars indicate 95% confidence intervals on log-normal distributions.
}

and current velocity measurements (McPhee-Shaw et al. 2021; Kunze et al. 2012; Petruncio et al. 1997). Therefore, the observed relationship between h_w and L_{tr} should be interpreted as a bulk constraint, reflective of how the size of near boundary overturns was reflected in the thickness of intrusions resulting from boundary layer-interior exchange.

An alternate signature of exchange between the boundary layer and the interior is stratification anomalies resulting from the along-isopycnal transport of mixed water from the boundary. In a well-mixed intrusion, the buoyancy anomaly, relative to the initial condition, will be positive in the lower half of the intrusion and negative in the upper half, with related stratification anomalies (Fig. A1c, with details of the calculation given in Appendix B). The stratification anomaly thickness, L_{N^2}, in Fig. 11b also scaled linearly with effective wave height when averaged over several wave periods for each simulation. The organization of the stratification anomaly with h_w emphasizes the importance of diabatic processes in wave breaking and subsequent ejection. These results again indicate that water mixed along the lower boundary, with overturn size scaled by h_w, was ejected into the interior along isopycnals, setting the magnitude of this interior exchange and connecting the intrusion thickness to the along-boundary mixing.

d. Turbulent buoyancy fluxes

The ejection of mixed water from the boundary into the interior provides a pathway for maintaining efficient mixing, hence here we consider the associated water-mass transformation, as described by the divergence of buoyancy fluxes. Due to the nonlinear nature of the internal waves, it is convenient to decompose the perturbations into periodic wave and turbulent motions such that, (Reynolds and Hussain 1972)

$$b = \bar{b} + \tilde{b} + b'. \tag{9}$$

Here, $\bar{b}$ is the mean buoyancy field, where $\overline{(\cdot)}$ indicates temporal averaging over several wave periods, $\tilde{b}$ is the periodic portion of the buoyancy field found using the phase average, $\langle \cdot \rangle$,

$$\langle b \rangle = \bar{b} + \tilde{b}, \tag{10}$$

and b', as the residual, represents the turbulent motion. This triple decomposition using only temporal averaging results in the following equation for the evolution of the mean buoyancy,

$$\frac{\partial \bar{b}}{\partial t} + \bar{\mathbf{u}} \cdot \nabla \bar{b} = -\nabla \cdot \overline{(\tilde{\mathbf{u}}\tilde{b})} - \nabla \cdot \overline{(\mathbf{u}'b')} + \overline{\nabla \cdot \kappa \nabla b}, \tag{11}$$

where κ is the eddy diffusivity calculated using the LES closure.

The flux divergences from the right-hand side of (11) are shown in Fig. 12. The non-linear wave term dominated over the turbulent term, though there was little difference between the two in sign throughout the near-slope domain. Directly above the topography, there was a thin layer, ~ 20 m thickness, where the vertical flux convergence was positive. Similar boundary convergence has been speculated to be important for upwelling in the abyssal circulation, however critically here we note that this region of vertical flux convergence was matched by a *horizontal* flux divergence.

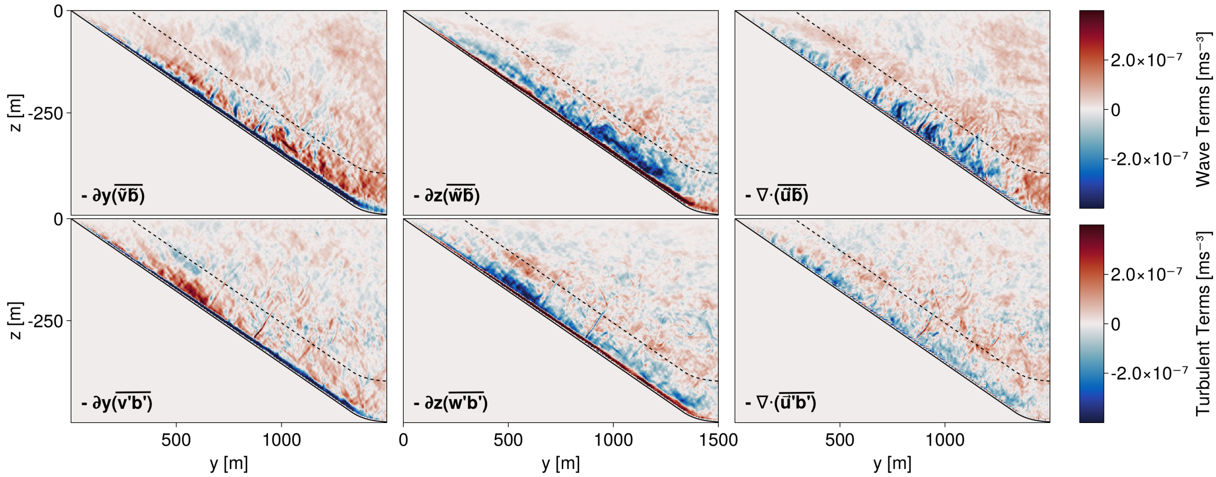

FIG. 12. Wave-averaged buoyancy fluxes indicate the similar magnitude importance of the horizontal and vertical buoyancy fluxes to mixing along the slope, as well as a relationship between the mixed region and effective wave height, h_w, where the dashed line is one h_w above the slope. The nonlinear wave effects dominate the buoyancy evolution, but both flux terms show near-boundary buoyancy flux divergence.

Further from the topography, the vertical flux convergence was negative, but partially offset by positive horizontal flux convergence. Notably, in a rotated coordinate system, the slope-normal component did not have the same convergent boundary region pattern as the vertical buoyancy flux, indicating the importance of the portion of the horizontal buoyancy flux that projects on the slope-normal direction. These results indicate the total buoyancy flux was divergent near the boundary, with convergence in the interior above the wave-breaking region, as seen in the total $-\nabla\cdot(\overline{\tilde{\mathbf{u}}\tilde{b}})$ in Fig. 12 (which we note is coordinate-agnostic). The effective wave height shown to scale the breaking and exchanges also scaled the height above boundary where the buoyancy flux divergence occurred (dashed line in Fig. 12).

The vertical buoyancy flux is often assumed to be the dominating component in boundary mixing, but these numerical results suggest both horizontal and vertical components could play a significant role due to the order-1 aspect ratio of overturns and the development of horizontal buoyancy gradients during the wave breaking events (Fig. 3). Buoyancy flux plots of 2D tidal simulations by Ruan and Ferrari (2023) also show horizontal and vertical fluxes of similar magnitude, though the relatively large ratio of h_w to grid-spacing in their simulations may have resulted in under-resolved wave-breaking overturns. The order-1 aspect ratio in horizontal and vertical flux variations

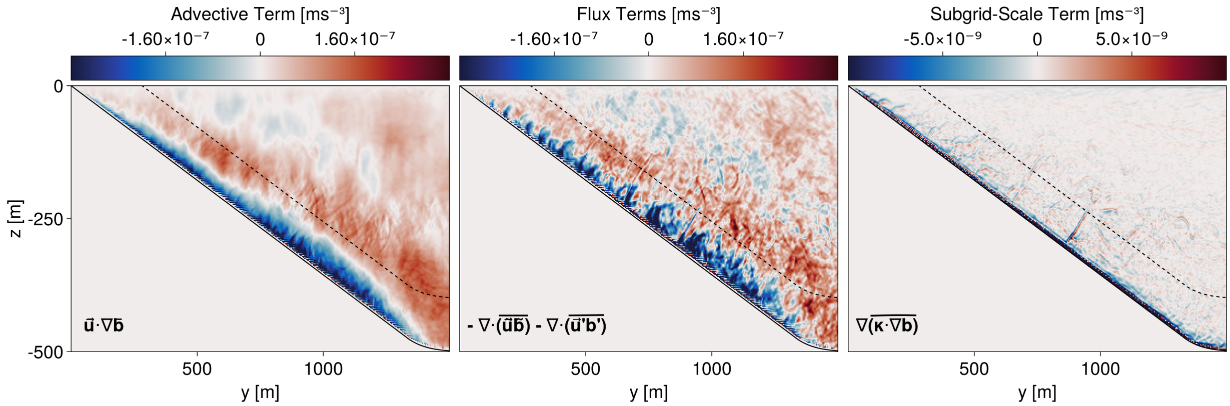

FIG. 13. Wave-averaged buoyancy budget terms show good agreement between the wave-averaged advective term and the buoyancy fluxes in a steady-state solution. The subgrid-scale term is negligible.

indicated the horizontal buoyancy flux divergence could not be neglected in these simulations (cf., Holmes and McDougall 2020). By considering both components, the near-boundary buoyancy flux convergence was canceled out entirely, and the remaining divergence within the overturning region was less than that of the vertical component alone.

The total buoyancy flux convergence in (11) was primarily balanced by mean buoyancy advection, such that $\partial\bar{b}/\partial t \approx 0$ (Fig. 13). This implies a mean downwelling along the topography, again emphasizing the role of the horizontal buoyancy flux in canceling the thin layer of vertical buoyancy flux convergence near the bottom. However, it is important to note that the mean buoyancy did not reach a steady state during these simulations. Fig. 14a shows wave-averaged buoyancy (gray contours), compared to the initial condition with uniform stratification (black contours). The water at the top of the slope was getting denser, while water at the bottom of the slope got lighter, indicating a convergence of mass into intermediate buoyancy classes. This signature continued to intensify throughout these simulations. Compared to the relative uniformity along the slope of the buoyancy flux divergence in Fig. 13, the total change in wave-averaged buoyancy was much more dependent on the location of the initial buoyancy class along the slope. While the mean buoyancy budget suggests net downwelling near the boundary, the total change in buoyancy over time indicates there is variable water-mass transformation with a spatially dependent up- and downwelling pattern along the slope.

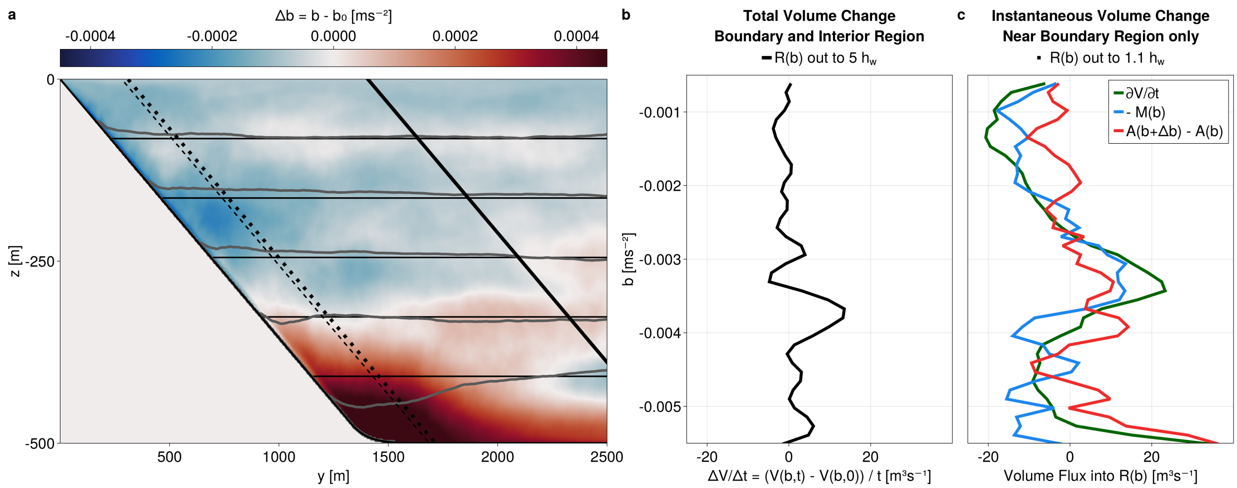

FIG. 14. (a) shows the change in wave-averaged buoyancy, $\bar{b}$, (gray contours) compared to the initial condition, b_0, (black contours). Contours represent isopycnals at 10^{-3} ms^{-2} intervals, and the thin dashed line is $1\,h_w$ from the slope, with buoyancy decreasing at the top and increasing at the bottom. Plot (b) shows the integrated volume change in buoyancy space from (a), normalized by the change in time, where H is marked in (a) as the thick solid line, $5\,h_w$ from the slope. Plot (c) shows the instantaneous volume budget from (8) over a region extending $1.1h_w$ from the slope, with the near-boundary diapycnal buoyancy flux (red) matching the intermediate buoyancy class experiencing convergence (a) and an increase in volume in (b). All plots are wave-averaged over the same range as the phase averages in Fig. 10, waves 4 - 10.

The residual in the buoyancy-binned volume budget (Fig. 10f) also indicated a phase-dependent diapycnal volume flux through the isopycnal surfaces, $A(b+\Delta b) - A(b)$. Diapycnal fluxes into near-boundary buoyancy classes occurred near the transition from upslope to downslope flow. While the breaking was strongest during the downslope phase, the stratification was also weakest during this phase, allowing for a difference in phase between the strongest diapycnal fluxes and the peak of the breaking event (Fig. 10b,c). The wave-averaged near-boundary volume budget shown in Fig. 14c for the same simulation indicates a net gain of volume in the near boundary region through isopycnal surfaces around $b = -0.003$ and -0.004 ms^{-2}. This volume change was not as large as that of the interior-exterior transport, as that is largely balanced by reversible changes in near-boundary volume. Extending the binned region out to $5h_w$ (the thick black line in Fig. 14a), the total change in volume ΔV, normalized by the difference of time, indicated a convergence of mass into a similar buoyancy class, shown in Fig. 14b. By including interior waters, the volume changes ignored the impact of along-isopycnal motions close to the boundary, focusing on the irreversible volume fluxes. These increases culminated in a buoyancy class that is 90% larger than it was initially. In physical space, this buoyancy class was also near the transition between the regions getting denser and lighter in Fig. 14a.

These results can be synthesized as follows. During the breaking events boundary fluid was mixed on time scales much smaller than a wave period, with brief moments of intense mixing and interior exchange in response to the strong downslope flow and the upslope dense bore (Fig. 10). The timing of water-mass transformation during the wave breaking was not necessarily coincident with the strongest kinetic energy dissipation rates, as stratification and turbulence covary (Fig. 10f and Cyr and van Haren 2016). In the time-mean, this led to a pattern of buoyancy flux divergence within $\sim 1\, h_w$ of the boundary, with horizontal flux divergences playing a significant role in the total (Figs. 12, 13). This flux divergence was largely balanced by mean downslope advection (Fig. 13), however, the simulations were not in steady state, such that there was an ongoing convergence of mass into intermediate density classes (Fig. 14). Determining to what extent these results are dependent on our numerical configuration (both domain size and treatment as an initial value problem), and what selects the convergent buoyancy class more generally in realistic settings is beyond the scope of the present work. However, the results presented here offer guidance towards interpreting observations, particularly highlighting the role of lateral fluxes, the dependence of diapycnal volume fluxes on along-slope position, and the subsequent ejection of mixed waters into the interior along-isopycnals.

4. Conclusion

Three-dimensional LES were used to demonstrate the relationship between breaking internal waves on sloping topography, overturn size, and along-isopycnal intrusions, through the *effective wave height*, h_w. The simulations indicated there were two main wave breaking points within the wave period. The internal waves overturned and broke when the downslope velocity was strongest, which was followed by the rapid appearance of a dense, upslope bore and the next overturn event (Fig. 3). Such overturns are often seen in observations and other numerical simulations (Aucan et al. 2006; Cyr and van Haren 2016; Winters 2015; van Haren and Gostiaux 2012a; Gayen and Sarkar 2011). Our results suggest the effective wave height, h_w, defined as the ratio of wave velocity to background buoyancy frequency (4), governed the scale of the overturns found along the slope as well as the resulting dissipation rate of kinetic energy (Figs. 5, 6).

After mixing boundary waters, the strong stratification at the head of the upslope bore forced the mixed fluid into the interior. This lateral pumping with ejections into the interior between the most energetic breaking downslope phase and the strongly stratified upslope phase is shown in Fig. 10. The effect of the near-boundary wave breaking was communicated into the interior through these along-isopycnal intrusions, with tracer intrusion thicknesses again scaled by the effective wave height, h_w (Fig. 11a and see Winters 2015). During a breaking event, fluid was mixed over a near-boundary layer approximately 1 h_w thick and was subsequently ejected into the interior, resulting in stratification anomaly thicknesses in the interior also scaled by the effective wave height (Fig 11b). There is variability in the thickness of individual intrusions (in both time and space), however h_w provides a useful bulk diagnostic and provides a connection between physical processes, from the near-boundary overturns to the boundary layer - interior exchanges and diapycnal mixing.

The total buoyancy flux averaged over several wave periods (Fig. 12) showed especially strong divergence within the overturning region extending a height of approximately h_w above the slope. In this region, both horizontal and vertical buoyancy fluxes contributed significantly to the total flux divergence, a consequence of the order-1 aspect ratio of overturning features along with the development of strong horizontal buoyancy gradients that preceded breaking events. While this near-slope divergence was mainly balanced by mean downslope advection (Fig. 13), a volume budget in buoyancy space shows there was a net diapycnal flux into intermediate buoyancy classes along the slope, with a convergence of mass due to adiabatic exchanges in nearby buoyancy classes as well (Fig. 14). The net diapycnal flux was driven by short bursts of intense mixing within a wave phase (Fig. 10), at the transition between the upslope and downslope phases. Covariances of turbulent dissipation and stratification anomalies (Fig. 14 b,c), along with the role of lateral fluxes (Fig. 12), suggest caution in the interpretation of vertical profile data or the use of time-averaged fields to infer the resulting water mass transformation.

How these results change in the presence of a more realistic slope geometry and internal wavefield—including variations in slope criticality, bottom roughness, 3D bathymetry such as canyons, and time-varying wave forcing—is an open question with important implications for understanding the net mixing during these types of breaking events. Likewise, the Lagrangian watermass evolution, in the presence of near-boundary mixing and strong interior-boundary layer exchanges could be usefully considered in future work. Results presented here give insight into the turbulent mixing generated by waves breaking on topography and suggest that the effective wave height, h_w, provides a useful constraint on wave energetics that can be applied to understanding the near-boundary breaking zone, adiabatic exchanges of mixed-fluid with the interior, and the rate of turbulent dissipation.

Acknowledgments. The authors thank Gregory L. Wagner, Ali Ramadhan, and Gabriel Weymouth for assistance in implementing the immersed boundary method in Oceananigans (Ramadhan et al. 2020), and Tomás Chor for advice on model setup and diagnostics. Three anonymous reviewers are also thanked for their comments. This material is based upon work supported by the National Science Foundation under Grant Numbers OCE-1948953 and OCE-2232441.

Data availability statement. Model configuration and analysis scripts will be made publicly available via github.com before manuscript publication.

APPENDIX A

Numerical calculation of tracer intrusion thickness

The thickness of interior dye intrusions is calculated for each simulation. At every time step the tracer concentration, initialized as a hyperbolic tangent function along the entire slope, is averaged in x, and smoothed in y via a rolling window of 40 grid points, as shown in Fig. A1 a for a representative time step. For each vertical profile of the tracer, the numerical derivative with respect to z is used to find all local minima in the profile. If the sign of the derivative changes from negative to positive, then the concentration has reached a minimum, indicating a possible boundary for an intrusion. The near-slope region is excluded by removing points within 6 m of the slope, to avoid including the bottom boundary layer itself in the calculation of intrusion thickness.

As can be inferred from the profile in Fig. A1b, the minima found are not always relevant. The local minima could just be a slight change in concentration within a much larger intrusion, or it could be a minima corresponding to an intrusion with very low concentration. To avoid such cases, intrusions are only included from a dye profile if the maximum concentration within a candidate intrusion reaches a threshold of 10^{-4}, and its bordering minimums dropped at least half the concentration of the maximum. Such examples can be seen marked by the blue markers in Fig. A1b. For example, if the maximum concentration of an intrusion in a certain dye profile is 10^{-3}, then the bordering minima would have to be less than 5×10^{-4} to include that intrusion in the average. The thickness of each intrusion is then measured above a 10^{-6} cutoff concentration of dye in the profile. So, even if the minimums surrounding an intrusion dropped to 0 concentration, the thickness would only measure to where the concentration had dropped to 10^{-6}.

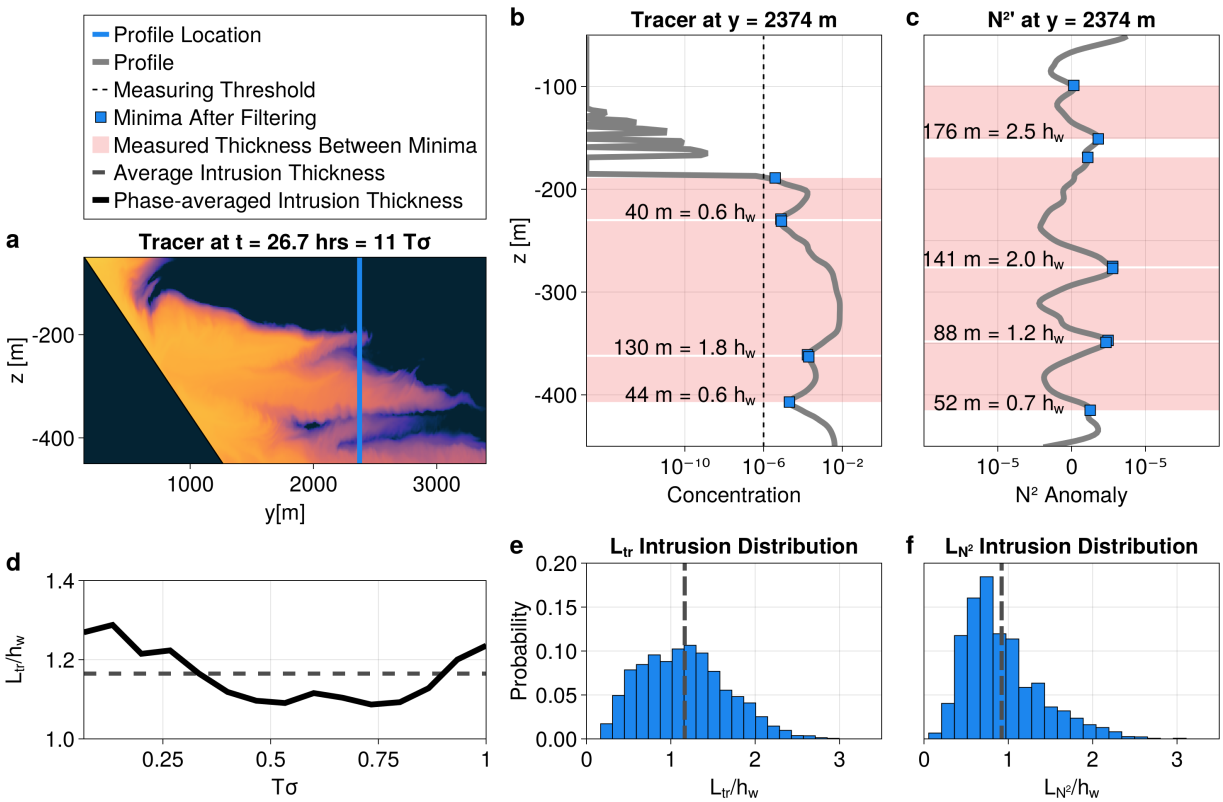

FIG. A1. Depiction of intrusion thickness in a representative profile. (a) tracer concentration at $t = 11T_\sigma$, after the initial smoothing, discussed in Appendix A. (b) the vertical profile of the tracer concentration taken at the location marked by the blue line in (a). The dashed line indicates the threshold for allowable values of concentration used in the calculation. (c) the vertical profile of stratification anomalies at the same location. Red shaded regions indicate an included intrusion calculation for either measure, with blue markers at the endpoints. (d) The phase-averaged tracer intrusion thickness normalized by the simulation's h_w shows temporal variation around the mean. Probability distributions of all included tracer intrusions (e) and stratification anomaly intrusions (f).

Once bounds are identified on the intrusions, the thickness can be easily found as the difference between the two minimums. The thickness of three such intrusions is marked in Fig. A1b by the red regions. All of these accepted intrusion thicknesses were averaged in space for each time step, and then in time over the last 5 wave periods to get an average intrusion thickness for each simulation. This is the value used in Fig. 11.

Various other methods and criteria for extracting intrusion thickness were also tested and the results were found to be qualitatively insensitive. As discussed in the text, we are primarily interested in characterizing the bulk variability, which we do using the mean, however, the median of the estimated tracer intrusion thickness gives similar results. There is however a large amount of variation in the estimated intrusion thickness within a single simulation, as can be seen by the three intrusions measured in Fig. A1b, and the histogram of all of the measured intrusions for the full simulation in Fig. A1e, especially for larger values of h_w. This variability is a function of both space (where for example position along the slope may lead to different intrusion thicknesses), wave phase as evidenced by the near boundary volume budget depicted in Fig. 14, as well as potentially a simple consequence of the turbulent breakdown of the large overturns which will energize a range of different scales. The adiabatic pumping of near boundary fluid will impact the amount of tracer captured in the interior as well as the average thickness. The phase-averaged intrusion thickness is shown in Fig. A1d, varying $\pm 0.1 h_w$ around the total mean within a wave phase. Error estimates on the mean are calculated assuming a log-normal distribution (Fig. A1), and treating snapshots in time (but not space) as providing independent degrees of freedom. The confidence intervals in Fig. 11 indicate that despite a large amount of variability, the scaling argument shown in the linear relationship still holds.

APPENDIX B

Numerical calculation of interior stratification anomaly thickness

Stratification anomalies can also be used to define the thickness of intrusions, using the instantaneous N^2 values calculated in each simulation. The stratification anomaly is defined as $N^{2\prime} = N^2 - N_0^2$. To smooth the resulting values, a rolling average in y of over 41 grid points, and in z of 7 grid points is taken. To avoid the impact of the internal wave forcing, a rolling wave average is taken over one wave period as well. For the smallest h_w, as well as for the subcritical cases, this averaging is not enough, and we are unable to extract the impact of the mixing events from the regular wave patterns. Hence, these results are not included in Fig. 11b. For each time step, and each vertical profile, we find all the indices for the negative values of $N^{2\prime}$, above the same slope cutoff described in the previous section. Intervals of consecutive indices indicate the vertical extent of the stratification anomaly. The full range of a well-mixed intrusion will also include small positive regions on either side of the negative anomaly. To capture these, the first positive peak in stratification anomaly on either side of the negative range is taken to be the end points of the intrusion. An example of such a profile with the measured intrusions can be seen in Fig A1c. After averaging over all the calculated thicknesses at a given time step, we again average in time over the last 4 waves (rolling wave average removes the last wave as a possibility) to find an average intrusion thickness for each simulation. The distribution of captured intrusion thicknesses for this method can be seen in Fig. A1f, with the mean over the whole simulation marked by the gray dashed line. While there is again a lot of variability, the uncertainty calculation, shown by the 95th percent confidence intervals in Fig. 11b, indicates the scaling is robust.

References

Alford, M. H., and Coauthors, 2011: Energy flux and dissipation in luzon strait: Two tales of two ridges. *Journal of Physical Oceanography*, **41**, 2211–2222, https://doi.org/10.1175/JPO-D-11-073.1.

Alford, M. H., and Coauthors, 2024: Buoyancy flux and mixing efficiency from direct, near-bottom turbulence measurements in a submarine canyon. *Submitted to J. Phys. Oceanogr.,*.

Armi, L., 1978: Some evidence for boundary mixing in the deep ocean. *Journal of Geophysical Research*, **83**, 1971, https://doi.org/10.1029/JC083iC04p01971.

Aucan, J., M. A. Merrifield, D. A. Luther, and P. Flament, 2006: Tidal mixing events on the deep flanks of kaena ridge, hawaii. *Journal of Physical Oceanography*, **36**, https://doi.org/10.1175/JPO2888.1.

Balmforth, N. J., and W. R. Young, 2002: Tidal conversion by subcritical topography. *Journal of Physical Oceanography*, **32**, 2900–2914.

Bonnin, J., H. van Haren, P. Hosegood, and G.-J. A. Brummer, 2006: Burst resuspension of seabed material at the foot of the continental slope in the rockall channel. *Marine Geology*, **226**, 167–184, https://doi.org/10.1016/j.margeo.2005.11.006.

Cacchione, D. A., and D. E. Drake, 1986: Nepheloid layers and internal waves over continental shelves and slopes. *Geo-Marine Letters*, **6**, https://doi.org/10.1007/BF02238085.

Chalamalla, V. K., B. Gayen, A. Scotti, and S. Sarkar, 2013: Turbulence during the reflection of internal gravity waves at critical and near-critical slopes. *Journal of Fluid Mechanics*, **729**, 47–68, https://doi.org/10.1017/jfm.2013.240.

Cheriton, O. M., E. E. McPhee-Shaw, W. J. Shaw, T. P. Stanton, J. G. Bellingham, and C. D. Storlazzi, 2014: Suspended particulate layers and internal waves over the southern monterey bay continental shelf: An important control on shelf mud belts? *Journal of Geophysical Research: Oceans*, **119**, https://doi.org/10.1002/2013JC009360.

Churchill, J. H., P. E. Biscaye, and F. Aikman, 1988: The character and motion of suspended particulate matter over the shelf edge and upper slope off cape cod. *Continental Shelf Research*, **8**, https://doi.org/10.1016/0278-4343(88)90077-5.

Cyr, F., and H. van Haren, 2016: Observations of small-scale secondary instabilities during the shoaling of internal bores on a deep-ocean slope. *Journal of Physical Oceanography*, **46**, 219–231, https://doi.org/10.1175/JPO-D-15-0059.1.

Dillon, T. M., 1982: Vertical overturns: A comparison of thorpe and ozmidov length scales. *Journal of Geophysical Research*, **87**, https://doi.org/10.1029/jc087ic12p09601.

Drake, H. F., R. Ferrari, and J. Callies, 2020: Abyssal circulation driven by near-boundary mixing: Water mass transformations and interior stratification. *Journal of Physical Oceanography*, **50**, 2203–2226, https://doi.org/10.1175/JPO-D-19-0313.1.

Drazin, P. G., 1961: On the steady flow of a fluid of variable density past an obstacle. *Tellus*, **13**, 239–251, https://doi.org/10.1111/j.2153-3490.1961.tb00081.x.

Edge, W. C., N. L. Jones, M. D. Rayson, and G. N. Ivey, 2021: Calibrated suspended sediment observations beneath large amplitude non-linear internal waves. *Journal of Geophysical Research: Oceans*, **126**, https://doi.org/10.1029/2021JC017538.

Eriksen, C. C., 1985: Implications of ocean bottom reflection for internal wave spectra and mixing. *Journal of Physical Oceanography*, **15**, https://doi.org/10.1175/1520-0485(1985)015⟨1145:ioobrf⟩2.0.co;2.

Ferrari, R., A. Mashayek, T. J. McDougall, M. Nikurashin, and J. M. Campin, 2016: Turning ocean mixing upside down. *Journal of Physical Oceanography*, **46**, https://doi.org/10.1175/JPO-D-15-0244.1.

Gardner, W. D., B. E. Tucholke, M. J. Richardson, and P. E. Biscaye, 2017: Benthic storms, nepheloid layers, and linkage with upper ocean dynamics in the western north atlantic. *Marine Geology*, **385**, 304–327, https://doi.org/10.1016/j.margeo.2016.12.012.

Gayen, B., and S. Sarkar, 2011: Boundary mixing by density overturns in an internal tidal beam. *Geophysical Research Letters*, **38**, https://doi.org/10.1029/2011GL048135.

Gemmrich, J., and J. M. Klymak, 2015: Dissipation of internal wave energy generated on a critical slope. *Journal of Physical Oceanography*, **45**, 2221–2238, https://doi.org/10.1175/JPO-D-14-0236.1.

Gill, A. E., 1982: *Atmosphere-Ocean Dynamics*, Vol. 110. Academic Press, 280-281 pp., https://doi.org/10.1002/qj.49711046322.

Holmes, R. M., and T. J. McDougall, 2020: Diapycnal transport near a sloping bottom boundary. *Journal of Physical Oceanography*, **50**, https://doi.org/10.1175/JPO-D-20-0066.1.

Hopfinger, E. J., 1987: Turbulence in stratified fluids: A review. *Journal of Geophysical Research*, **92**, 5287, https://doi.org/10.1029/JC092iC05p05287.

Jalali, M., V. K. Chalamalla, and S. Sarkar, 2017: On the accuracy of overturn-based estimates of turbulent dissipation at rough topography. *Journal of Physical Oceanography*, **47**, 513–532, https://doi.org/10.1175/JPO-D-15-0169.1.

Jalali, M., and S. Sarkar, 2017: Large eddy simulation of flow and turbulence at the steep topography of luzon strait. *Geophysical Research Letters*, **44**, 9440–9448, https://doi.org/10.1002/2017GL074119.

Jones, N. L., G. N. Ivey, M. D. Rayson, and S. M. Kelly, 2020: Mixing driven by breaking nonlinear internal waves. *Geophysical Research Letters*, **47**, https://doi.org/10.1029/2020GL089591.

Kaiser, B. E., L. J. Pratt, and J. Callies, 2022: Low-reynolds-number oscillating boundary layers on adiabatic slopes. *Journal of Fluid Mechanics*, **950**, A4, https://doi.org/10.1017/jfm.2022.794.

Khani, S., 2018: Mixing efficiency in large-eddy simulations of stratified turbulence. *Journal of Fluid Mechanics*, **849**, 373–394, https://doi.org/10.1017/jfm.2018.417.

Klymak, J. M., S. Legg, M. H. Alford, M. Buijsman, R. Pinkel, and J. D. Nash, 2012: The direct breaking of internal waves at steep topography. *Oceanography*, **25**, 153–159, https://doi.org/10.5670/oceanog.2012.50.

Kunze, E., C. Mackay, E. E. Mcphee-Shaw, K. Morrice, J. B. Girton, and S. R. Terker, 2012: Turbulent mixing and exchange with interior waters on sloping boundaries. *Journal of Physical Oceanography*, **42**, 910–927, https://doi.org/10.1175/JPO-D-11-075.1.

Lamb, K. G., 2014: Internal wave breaking and dissipation mechanisms on the continental slope/shelf. *Annual Review of Fluid Mechanics*, **46**, 231–254, https://doi.org/10.1146/annurev-fluid-011212-140701.

Legg, S., and J. Klymak, 2008: Internal hydraulic jumps and overturning generated by tidal flow over a tall steep ridge. *Journal of Physical Oceanography*, **38**, 1949–1964, https://doi.org/10.1175/2008JPO3777.1.

Marshall, J., A. Adcroft, C. Hill, L. Perelman, and C. Heisey, 1997: A finite-volume, incompressible navier stokes model for studies of the ocean on parallel computers. *J. Geophys. Res.*, **102**, 5753–5766.

Marshall, J., D. Jamous, and J. Nilsson, 1999: Reconciling thermodynamic and dynamic methods of computation of water-mass transformation rates. *Deep Sea Research I*, **46**, 545–572.

Mashayek, A., R. Ferrari, S. Merrifield, J. R. Ledwell, L. S. Laurent, and A. N. Garabato, 2017: Topographic enhancement of vertical turbulent mixing in the southern ocean. *Nature Communications*, **8**, 14 197, https://doi.org/10.1038/ncomms14197.

Mater, B. D., S. M. Schaad, and S. K. Venayagamoorthy, 2013: Relevance of the thorpe length scale in stably stratified turbulence. *Physics of Fluids*, **25**, https://doi.org/10.1063/1.4813809.

Mater, B. D., S. K. Venayagamoorthy, L. S. Laurent, and J. N. Moum, 2015: Biases in thorpe-scale estimates of turbulence dissipation. part i: Assessments from large-scale overturns in oceanographic data. *Journal of Physical Oceanography*, **45**, 2497–2521, https://doi.org/10.1175/JPO-D-14-0128.1.

McPhee-Shaw, E., 2006: Boundary–interior exchange: Reviewing the idea that internal-wave mixing enhances lateral dispersal near continental margins. *Deep Sea Research Part II: Topical Studies in Oceanography*, **53**, 42–59, https://doi.org/10.1016/j.dsr2.2005.10.018.

McPhee-Shaw, E., R. Sternberg, B. Mullenbach, and A. Ogston, 2004: Observations of intermediate nepheloid layers on the northern california continental margin. *Continental Shelf Research*, **24**, 693–720, https://doi.org/10.1016/j.csr.2004.01.004.

McPhee-Shaw, E. E., and E. Kunze, 2002: Boundary layer intrusions from a sloping bottom: A mechanism for generating intermediate nepheloid layers. *Journal of Geophysical Research*, **107**, https://doi.org/10.1029/2001jc000801.

McPhee-Shaw, E. E., E. Kunze, and J. B. Girton, 2021: Submarine canyon oxygen anomaly caused by mixing and boundary-interior exchange. *Geophysical Research Letters*, **48**, https://doi.org/10.1029/2021GL092995.

Nielson, J. R., and S. M. Henderson, 2022: Bottom boundary layer mixing processes across internal seiche cycles: Dominance of downslope flows. *Limnology and Oceanography*, **67**, 1111–1125, https://doi.org/10.1002/lno.12060.

Nokes, R. L., and G. N. Ivey, 1989: Vertical mixing due to the breaking of critical internal waves on sloping boundaries. *Journal of Fluid Mechanics*, **204**, https://doi.org/10.1017/S0022112089001849.

Petruncio, E. T., L. K. Rosenfeld, and J. D. Paduan, 1997: Observations of the internal tide in monterey canyon. *Journal of Physical Oceanography*.

Polzin, K. L., J. M. Toole, J. R. Ledwell, and R. W. Schmitt, 1997: Spatial variability of turbulent mixing in the abyssal ocean. *Science*, **276**, 93–96.

Ramadhan, A., and Coauthors, 2020: Oceananigans.jl: Fast and friendly geophysical fluid dynamics on gpus. *Journal of Open Source Software*, **5**, 2018, https://doi.org/10.21105/joss.02018.

Reynolds, W. C., and A. K. Hussain, 1972: The mechanics of an organized wave in turbulent shear flow. part 3. theoretical models and comparisons with experiments. *Journal of Fluid Mechanics*, **54**, https://doi.org/10.1017/S0022112072000679.

Ruan, X., and R. Ferrari, 2023: Diapycnal upwelling driven by tidally-induced mixing over steep topography. [preprint]. 239–251.

Sarkar, S., and A. Scotti, 2017: From topographic internal gravity waves to turbulence. *Annual Review of Fluid Mechanics*, **49**, 195–220, https://doi.org/10.1146/annurev-fluid-010816-060013.

Scorer, R. S., 1949: Theory of waves in the lee of mountains. *Quarterly Journal of the Royal Meteorological Society*, **75**, 41–56, https://doi.org/10.1002/qj.49707532308.

Silvestri, S., G. L. Wagner, J.-M. Campin, N. C. Constantinou, C. N. Hill, A. N. Souza, and R. Ferrari, 2024: A new weno-based momentum advection scheme for simulations of ocean mesoscale turbulence. *Journal of Advances in Modeling Earth Systems*, https://doi.org/10.22541/essoar.170110657.76489860/v2.

Slinn, D. N., and J. J. Riley, 1998: Theoretical and computational fluid dynamics turbulent dynamics of a critically reflecting internal gravity wave 1. *Theoret. Comput. Fluid Dynamics*, **11**, 281–303.

Thorpe, S., and M. White, 1988: A deep intermediate nepheloid layer. *Deep Sea Research Part A. Oceanographic Research Papers*, **35 (9)**, 1665–1671, https://doi.org/https://doi.org/10.1016/0198-0149(88)90109-4.

Thorpe, S. A., 1977: Turbulence and mixing in a scottish loch. *Philosophical Transactions of the Royal Society of London*, **286**, 125–181.

van Haren, H., 2006: Nonlinear motions at the internal tide source. *Geophysical Research Letters*, **33**, 2006GL025 851, https://doi.org/10.1029/2006GL025851.

van Haren, H., 2023: Kmt, detailing layered mixing governed by internal wave breaking. *Environmental Fluid Mechanics*, **23**, 603–620, https://doi.org/10.1007/s10652-023-09921-5.

van Haren, H., A. Cimatoribus, and L. Gostiaux, 2015: Where large deep-ocean waves break. *Geophysical Research Letters*, **42**, 2351–2357, https://doi.org/10.1002/2015GL063329.

van Haren, H., and L. Gostiaux, 2012a: Detailed internal wave mixing above a deep-ocean slope. *Journal of Marine Research*, **70**, 173–197.

van Haren, H., and L. Gostiaux, 2012b: Energy release through internal wave breaking. *Oceanography*, **25**, 124–131, https://doi.org/10.5670/oceanog.2012.47.

Winters, K. B., 2015: Tidally driven mixing and dissipation in the stratified boundary layer above steep submarine topography. *Geophysical Research Letters*, **42**, 7123–7130, https://doi.org/10.1002/2015GL064676.

Winters, K. B., and L. Armi, 2013: The response of a continuously stratified fluid to an oscillating flow past an obstacle. *Journal of Fluid Mechanics*, **727**, 83–118, https://doi.org/10.1017/jfm.2013.247.

Wynne-Cattanach, B. L., and Coauthors, 2024: Observations of diapycnal upwelling within a sloping submarine canyon. *Nature*, **630**, 884–890, https://doi.org/10.1038/s41586-024-07411-2.